

Synthesis of Bimetallic (Iron–Cobalt) Single Atom Catalysts for Electrochemical Detection of Nitrites

Guillermo Tostado-Blazquez,* Messaoud Harfouche, Jose L. Cerrillo, Abdullah Bukhamsin, Veerappan Mani, and Khaled Nabil Salama*

Nitrite (NO_2^-) is responsible for several physiological processes but can be harmful in excess. With rising exposure from food preservatives, fertilizers, and pollutants, accurate nitrite assessment is crucial for health and environmental safety. Different methods have been employed for its determination, with electrochemical sensors showcasing great promise. Single atom catalysts (SACs) are a class of nanomaterials that consists of isolated catalytic metal atoms anchored on conductive supports, which exhibit unique electronic properties with great promise for this application. The performance of these materials can be enhanced even more by incorporating a secondary metal in the catalyst structure. This leads to the creation of more surface-active sites and enables the facilitation of multi-step reactions. Herein, a bimetallic single atom catalyst (FeCoSAN) is synthesized through a single step laser assisted solid-process by anchoring iron and cobalt atoms while simultaneously creating a laser-scribed graphene (LSG) support. The presence of Fe and Co atoms is verified by high-angle annular dark-field scanning transmission electron microscopy (HAADF-STEM) and X-ray absorption spectroscopy (XANES and EXAFS). Through electrochemical testing, the bimetallic system demonstrated excellent capabilities for determination of NO_2^- , achieving up to 100% more efficiency, in comparison with bare LSG, with a detection limit of $2.42 \mu\text{M}$ and a sensitivity value of $515.07 \mu\text{A mm}^{-1} \text{cm}^{-2}$ over a linear range from 5.0 to $1666 \mu\text{M}$. This highlights their potential for in vivo and point-of-care sensing applications.

1. Introduction

Nitric oxide (NO) is a vital signaling molecule involved in numerous biological processes, such as vasodilation, platelet aggregation inhibition, angiogenesis, neurotransmission, immune response, and non-specific host defense.^[1] It is produced endogenously by a variety of mammalian cells, including neurons, macrophages, neutrophils, and platelets. As a membrane permeable species, it possesses the ability to diffuse throughout the vasculature, where it can interact with some reactive oxygen species (ROS), generating harmful radicals like peroxynitrite (ONOO^-), nitrite (NO_2^-) and nitrate (NO_3^-).^[2–4] Excessive production of these metabolites can lead to oxidative and nitrosative stress, promoting the development of conditions such as Parkinson's, Alzheimer's, atherosclerosis, hypotension, and chronic inflammation. Due to the short half-life of NO, its direct quantification is challenging. Therefore, the measurement of its stable by-products has been employed clinically to assess its presence.^[5]

G. Tostado-Blazquez, A. Bukhamsin, V. Mani, K. N. Salama
Sensors Lab
Bioengineering
Biological and Environmental Science and Engineering Division (BESE)
King Abdullah University of Science and Technology (KAUST)
Thuwal 23955, Saudi Arabia
E-mail: guillermo.tostadoblazquez@kaust.edu.sa;
khaled.salama@kaust.edu.sa

M. Harfouche
Synchrotron-light for Experimental Science and Applications in the
Middle East (SESAME)
PO Box 7, Allan 19252, Jordan

J. L. Cerrillo
KAUST Catalysis Center (KCC)
King Abdullah University of Science and Technology (KAUST)
Thuwal 23955, Saudi Arabia

V. Mani
Centre for Advanced Measurement Research & Health Translation
(CAMRHT)
Department of Pure and Applied Chemistry
University of Strathclyde
Glasgow G1 1XL, United Kingdom

 The ORCID identification number(s) for the author(s) of this article can be found under <https://doi.org/10.1002/admt.202401484>

© 2025 The Author(s). Advanced Materials Technologies published by Wiley-VCH GmbH. This is an open access article under the terms of the [Creative Commons Attribution-NonCommercial-NoDerivs License](#), which permits use and distribution in any medium, provided the original work is properly cited, the use is non-commercial and no modifications or adaptations are made.

DOI: 10.1002/admt.202401484

From those products, NO_2^- is of particular interest, as it is not only a key intermediate correlated to NO metabolism but also plays direct physiological roles in maintaining vascular homeostasis, modulating immune function, and influencing cellular signaling pathways. Physiological plasma levels of nitrite are in the range of 50–100 nM.^[6] Conversely, excessive nitrite levels have been linked to various pathological conditions, including cancer, and methemoglobinemia.^[7,8] In addition to the endogenous concentrations of this species, human exposure has rapidly increased in the last decade due to the employment of sodium nitrite (NaNO_2) as a food preservative, nitrogenous fertilizer for crops, and the presence of nitrites as atmospheric pollutants. Therefore, accurate quantification of nitrite is thus essential in both clinical diagnostics and environmental monitoring.^[9]

A wide array of techniques have been employed for the detection of nitrite in vivo. Among them, the Griess assay, a colorimetric method based on the diazotization reaction of nitrite, offers sensitivity in the micromolar range. However, it is prone to interference from other analytes in the blood and often requires complex sample preparation. As this test involves a color change arising from the formation of a pink-red azo dye, its sensitivity can be improved by coupling with other techniques, such as spectrophotometry, chemiluminescence and chromatography. Nonetheless, their practical application is still limited due to the expensive and bulky equipment needed in addition to the extensive sample processing time.^[10–12] A promising alternative arises in the form of electrochemical sensors, due to their simplicity of operation, rapid response, affordability, and potential for miniaturization.^[13] Nevertheless, conventional electrochemical sensors often suffer from poor selectivity and sensitivity at low nitrite concentrations, primarily due to the limited catalytic activity of the electrode materials.^[14]

Recently, single atom catalysts (SACs) has been reported to combine the advantages of high catalytic activity and selectivity, therefore, a step in the right direction for electrochemical sensors. In principle, isolated metal atoms anchored on a conductive support can act as SACs and due to their high atomic utilization, they exhibit unique electronic properties. The discreet nature of their active sites allows for precise modulation of the local electronic structure, rendering them a good option for nitrite detection.^[15–17] The catalytic performance of SACs can be further optimized through the development of bimetallic single atom systems. The presence of two different metal atoms in close proximity generates more available surface-active sites, enhancing catalytic performance, stability, and selectivity.^[18–20] Additionally, the incorporation of a secondary metal in the catalyst structure can be specifically designed to enhance the adsorption of a particular analyte, further enhancing the selectivity of the system or allowing for catalysis of multi-step reactions.^[21–24]

Different techniques and experimental procedures have been reported for the realization of bimetallic SACs, falling into a bottom-up or top-down category. The former consists in “building up” the catalyst from scratch through chemical reactions promoting ions and molecules to interact between them. Whereas the latter, it consists in “breaking down” larger structures, like supported nanoparticles or metallic salts, without damaging the scaffold. Some of the common limitations faced by these processes, in addition to the laborious multistep required, are aggregation, poor metal loading and low yield, limiting their further

application in biosensing.^[25,26] An alternative approach to this technique is offered by laser scribing. This solid-state synthesis can generate a graphitic support out of a carbon source material, while simultaneously introducing heteroatoms like N or O within the matrix, promoting the anchoring of the metal atoms via C–N–Metal coordination bonds. In addition to the simplicity of the technique, its low cost, versatility, and scalability positions it as great candidate for mass production.^[27,28]

In this study, we present for the first time a CO_2 laser-assisted solid-state synthesis of a bimetallic single-atom catalyst. The resulting material consists of a 3D porous graphene support with iron and cobalt atoms anchored as single atoms. Through electrochemical methods, we demonstrate the material's efficiency in the sensitive and selective determination of nitrite, mimicking the catalytic activity of nitrite oxidoreductase.

2. Results and Discussion

2.1. Characterizations

Figure 1 showcases the conducted experimental procedure for the synthesis of the bimetallic single atom catalyst (Fe-CoSAN), which is a modified version of our previously reported methods.^[29,30] Chiefly, a metallic slurry composed of iron chloride, cobalt nitrate, urea, and poly(vinyl alcohol) (PVA) was blade coated onto a polyimide (PI) substrate and annealed until a dry film was observed. Since a Metal–N–C coordination bond was desired to resemble a natural enzyme, the PI served as carbon source while the urea served as nitrogen source. The role of the PVA was as thickening agent since enhanced viscosity of the slurry was needed due to the poor wettability of the PI. Finally, the coated dry samples were irradiated with a CO_2 laser, inducing sudden and focalized temperature rises above 2500 °C, promoting the formation of a superficial porous graphitic matrix through the release of CO and CO_2 gases while simultaneously incorporating the immobilized metallic heteroatoms from the slurry within it.^[31]

Scanning electron microscope (SEM) was employed to study the morphology of the electrodes. Samples were sputtered with 3 nm of iridium to avoid charging effect. The acquired SEM images of the FeCoSAN electrode and a control LSG are presented in **Figure S1** (Supporting Information). In both cases, a 3D porous arrangement of vertically aligned sheets can be observed, suggesting that the anchoring of the metallic atoms on the support did not negatively influence its final structure.

Next, high-angle-annular dark-field scanning transmission electron microscopy (HAADF–STEM) was used to visualize the atomic dispersion of the metal atoms over the LSG support. As can be seen in **Figure 2a**, uniformly dispersed bright dots were observed, corresponding to either Co or Fe atoms. This technique is based on Z-contrast imaging, meaning that the intensity or the brightness of the atoms increases along with the atomic number (Z), however, since both metals are contiguous on the periodic table (Fe^{26} and Co^{27}), discerning their contrast signatures is practically not possible. In **Figure S2** (Supporting Information) three zoomed-in panels are presented where the diameter of the atoms was measured employing an image processing software (Thermo Scientific Velox). It can be appreciated that the atomic radii vary over a range of 128.0–159.9 pm, which falls within the theoretical

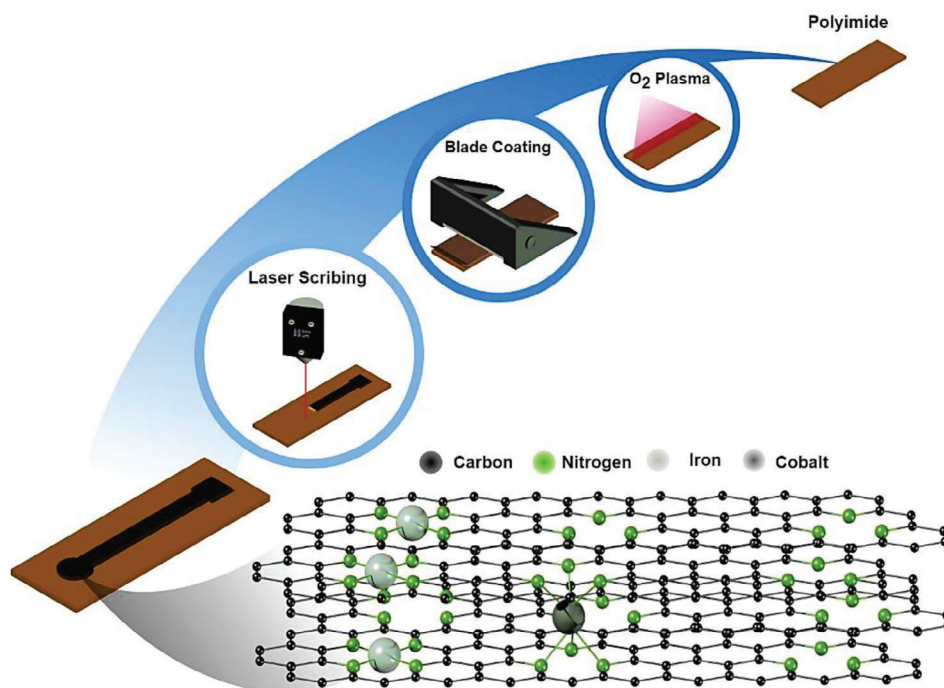


Figure 1. Experimental procedure of for the realization of the bimetallic single atom nanozyme (FeCoSAN).

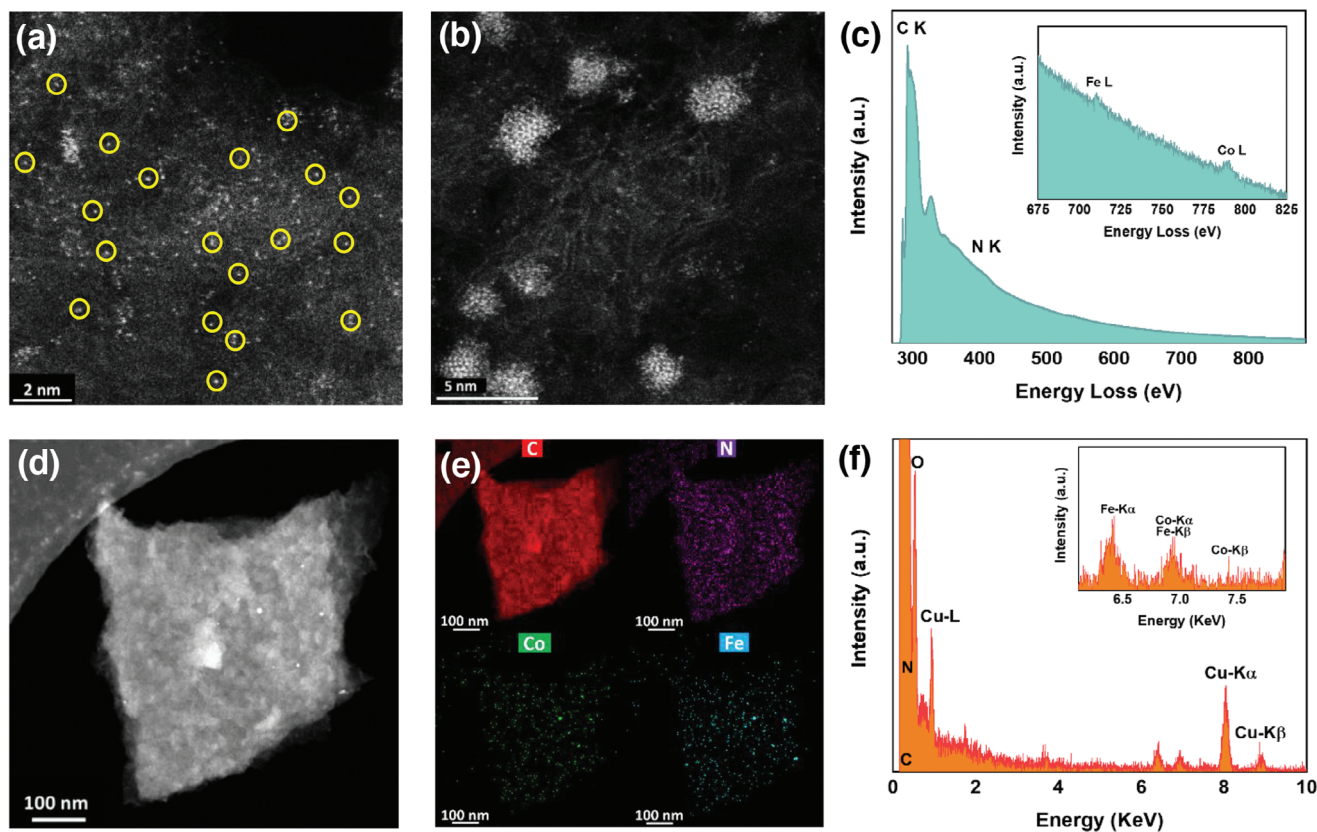


Figure 2. HAADF-STEM imaging of a) isolated Fe-Co Single atoms and b) clusters of iron and cobalt single atoms. c) EELS spectra of the FeCoSAN. d,e) EDS elemental mapping, and f) EDS spectra of the FeCoSAN electrode.

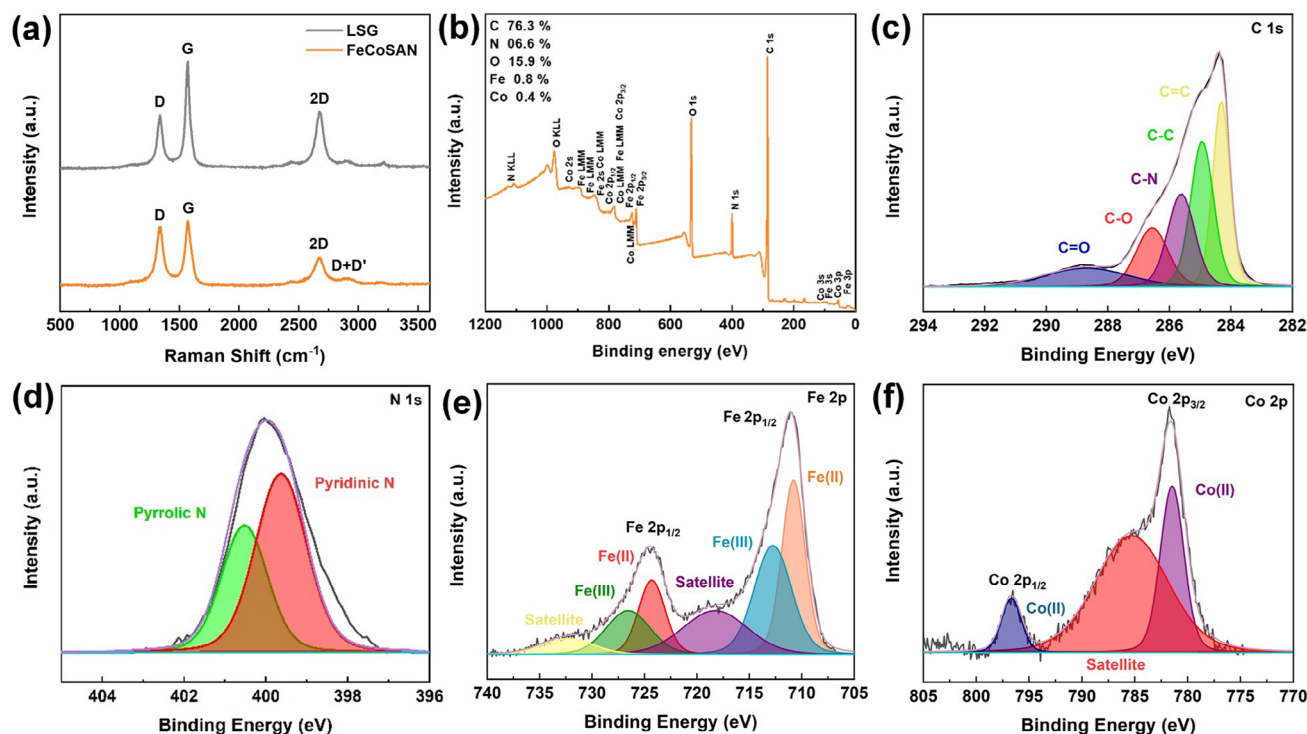


Figure 3. a) Raman spectra comparison between a bare LSG electrode and a FeCoSAN electrode. b) Survey XPS Scan of the FeCoSAN electrode with its corresponding high-resolution spectra of c) C 1s, d) N 1s, e) Fe 2p, and f) Co 2p.

value for iron and cobalt (126 and 152 pm respectively). In addition to the isolated single atoms, some other regions were appreciated where the atoms started to form clusters (Figure 2b) and even lattice fringes (Figure S3, Supporting Information). This could be attributed to the high ratio of iron in comparison with cobalt. Since Fe possess a higher magnetic moment, it can lead to the formation of clusters or agglomerates when exposed to high temperatures, like the ones produced by the laser.^[32] Through electron energy loss spectroscopy (EELS), the presence of iron and cobalt was confirmed by their characteristic core-loss edges. As can be seen on Figure 2c, the signal was quite muted, as it was expected since the test was conducted on regions of the material where single atoms were isolated. In order to obtain a better signal, additional measurements were carried out on some of the clusters (Figure S4, Supporting Information), where a clearer signal showcased the core loss edges of each element, in agreement with previous reports.^[33]

Moreover, energy-dispersive X-ray spectroscopy (EDS) was conducted to map-out the elemental distribution of C, N, O, Fe and Co and confirm its uniformity across the sample (Figure 2d,e). Furthermore, the elemental signatures of the major composing elements of the electrode were observed on the EDS spectra, in addition to the signal attributed to the copper grid where the sample was placed (Figure 2f).

Raman spectroscopy was employed to confirm the graphitic nature of the material and to verify the anchoring of the single atoms on the FeCoSAN in comparison with control bare LSG. The characteristic bands of graphite carbon were observed: D band at $\approx 1340\text{ cm}^{-1}$, G band at $\approx 1570\text{ cm}^{-1}$, and 2D band at $\approx 2670\text{ cm}^{-1}$ (Figure 3a). All three bands can serve as good indi-

cators of the morphology and nature of the sample. The D band is associated to the doping and defect density within the carbon lattice. The G band is related to the presence of sp^2 -hybridized carbon atoms and lastly, the 2D band is sensitive to the stacking order and number of layers in graphene. The prominent difference between the D and G bands of both samples can clearly be appreciated. The peak intensity ratio of D and G bands (I_D/I_G) was calculated for both, LSG and FeCoSAN, yielding values of 0.95 and 0.99, respectively, suggesting a higher number of defects on the FeCoSAN sample, attributed to the anchoring of the single atoms through C–N–Metal bonds. This is also supported by the rise of the D + D' band. Moreover, the peak intensity of the 2D and G bands (I_{2D}/I_G) was calculated to determine the density of graphene layers. The obtained values for LSG and FeCoSAN were 0.95 and 0.96 respectively, suggesting the presence of multiple graphene sheets, in concordance with the SEM images. In addition, it implies that the quality of the support was not drastically altered with the anchoring of the metallic atoms.

X-ray diffraction (XRD) was performed to study the crystallinity of the sample. As can be seen in Figure S5 (Supporting Information), the XRD patterns of bare LSG and FeCoSAN are almost identical, with two prominent peaks observed at 25.8° and 43.0° , attributed to the (002) and (100) graphitic crystal planes. Additionally, on the FeCoSAN spectra, two small peaks appeared at 30.0° and 35.4° which could be assigned to some characteristic planes of cobalt ferrite: (220) and (311).^[34] This confirms, that in fact, some of the clusters observed on STEM started to form fringes with crystalline components. It is important to highlight that no more peaks, aside from those previously mentioned, were to be found on the XRD patterns, suggesting that regardless of

the presence of some crystallographic planes, the clusters were not able to conform a full-sized nanoparticle.

X-ray photoelectron spectroscopy (XPS) was performed to confirm the surface composition of the sample and to probe the coordination environment and valence state of the metallic atoms. The survey scan revealed characteristic peaks for all the elements of interest (Figure 3b). The surface metal loading was determined to be $1.03 \pm 0.3\%$ $0.83 \pm 0.4\%$ for iron and cobalt respectively, based on the average of three different samples (Figure S6, Supporting Information). It's important to remark that the precision and accuracy on the elemental quantification of cobalt and iron is quite limited due to overlap of the main XPS peaks with the Auger peaks between both elements in addition to the small amount of metal available to quantify, reaching almost the limit of detection of the equipment. Moreover, high-resolution scans for each element were acquired (Figure 3c–f). The C 1s spectrum was deconvoluted into two homoatomic bands associated with sp^2 (284.3 eV) and sp^3 carbon (284.9 eV), in addition to three heteroatomic bonds C–N (285.6 eV), C–O (286.6 eV) and C=O (288.7 eV).^[35] The N 1s spectrum was resolved into two components positioned at 399.5 and 400.5 eV, assigned to pyridinic N and pyrrolic N, respectively, in concordance with the bands appreciated on the C 1s spectrum.^[36] The Fe 2p spectrum was deconvoluted into two sets of doublet peaks, assigned to Fe(II) (710.5 and 723.0 eV) and Fe(III) (714.5 and 726.3 eV) with the addition of a pair of satellites located at 718.1 and 732.3 eV, characteristic of the presence of Fe(III).^[37,38] Lastly, on the Co 2p spectrum, two prominent peaks were observed at 781.6 and 796.7, ascribed to the presence of Co(II), supported by the presence of a prominent satellite peak at 785.3 eV, arising from a shake-up process.^[39] A second satellite corresponding to the Co 2p $\frac{1}{2}$ could have been expected, however, it most likely got distorted due to the interactions between Co and Fe, according to the formation of some cobalt ferrite regions, as suggested by the XRD results.

X-ray absorption near-edge structure (XANES) and extended X-ray absorption fine structure (EXAFS) were performed to understand the coordination environment and chemical state of both, iron and cobalt atoms. As can be seen in Figure 4a, the linear combination fitting of the Fe K-edge XANES spectra of the FeCoSAN electrode rises before the Fe foil and between Fe(NO₃)₃ and FeCO₃, suggesting the existence of iron species with valences between Fe⁰ and Fe⁺³, in concordance with the results obtained from XPS. The calculated percentages of the redox states suggests the predominance of Fe(III) ($\approx 73.6\%$), with smaller contributions from Fe(0) ($\approx 19.0\%$) and Fe(II) ($\approx 7.4\%$). The reduced chi-square value (0.0009790) indicates a robust fit, further validating the results. The collected EXAFS data revealed Fe–C/N bonds with an average coordination number of 4.5 and a bond length of 2.00 Å, supporting the coordination of the metal atoms to the carbon support through nitrogen bonds (Figure 4b). Additionally, Fe–Fe bonds and Fe–Fe/Co bonds were revealed, confirming the presence of metal clusters or alloy-like structures in concordance with XRD results. Lastly, the Cauchy wavelet transform analysis further supports this, showing distinct features corresponding to Fe–C/N and Fe–Fe interactions, with overlapping regions suggesting the coexistence of both atomic dispersion and clusters (Figure 4c).

On the other hand, the linear combination fitting of the Co K-edge XANES spectra clearly rises before the Co foil and resem-

bles that of cobalt oxide, positioning Co²⁺ as the predominant species, in agreement with the findings from XPS measurements (Figure 4d). Once more, the percentages of the redox states were calculated suggesting Co(II) oxidation state ($\approx 97.8\%$), with minimal presence of Co(0) ($\approx 2.2\%$). The reduced chi-square value (0.0004779) indicates an accurate fit. Similarly to the Fe atoms, the EXAFS data supports the coordination of Co to the graphene support through nitrogen, as Co–C and/or Co–N bonds were revealed with an average coordination number of 6.5 at a distance of 2.07 Å (Figure 4e). Additionally, Co–O and Co–Fe bonds were found, supporting the presence of metal oxide alloys, further validating the XRD indexing of cobalt ferrite. The Cauchy wavelet transform revealed overlapping features, indicating a mixed environment with both atomically dispersed Co atoms and Co–Fe clusters (Figure 4f). Nonetheless, it's important to mention that regardless of the presence of this crystalline phase, based on the STEM results and the incomplete XRD patterns, we can claim that our synthesis predominantly synthesizes monoatomic distributions. The full EXAFS derived structural parameters around iron and cobalt are presented in Tables S1 and S2 (Supporting Information) respectively.

Inductively coupled plasma–optical emission spectroscopy (ICP-OES) was conducted to determine the bulk metal loading percentage of the sample. As can be seen on Table S3 (Supporting Information), the average values across samples for each metal are quite close from one another, suggesting a homogeneous blade-coating process. A total average of all three samples yielded a 1.135 ± 0.133 wt% of iron and 0.336 ± 0.046 wt% of cobalt loading with an average Fe:Co ratio of 3.3802. In comparison with the XPS results, the values obtained for Fe are quite close, however, for Co a discrepancy of $\approx 135\%$ was observed considering the results of ICP as the true values. This was expected, since, as it was previously mentioned, the accuracy of quantification through XPS for this particular bimetallic system is quite limited due to the overlapping of their spectra. On the other hand, since ICP-OES relies on selectively probing defined wavelengths associated with each element, instead of a full spectrum, the results can be considered more accurate.

2.2. Electrochemical Properties of FeCoSAN

The metal loading ratio of Fe:Co was optimized by varying the final concentrations of the metallic precursors, fabricating working electrodes with them and recording the differential pulse voltammetry (DPV) signal of the different samples in the presence of 500 μ M of NaNO₂. The first parameter to be optimized was the Fe loading. An initial concentration of 75 mM cobalt nitrate was fixed since it proved to be the most efficient system in a previous work. As can be seen in Figure S7a,b (Supporting Information), different versions of the catalyst were synthesized employing a ferric chloride final concentration of 25, 50, 75 and 100 mM. The best-performing system was obtained at 75 mM. Then, the cobalt loading was optimized by conducting the same procedure as with the iron precursor. The iron chloride concentration was fixed at 75 mM and the cobalt nitrate concentration was varied, yielding the best-performing material at a concentration of 25 mM, as can be seen in Figure S7c,d (Supporting Information). Finally, the best-performing material was determined

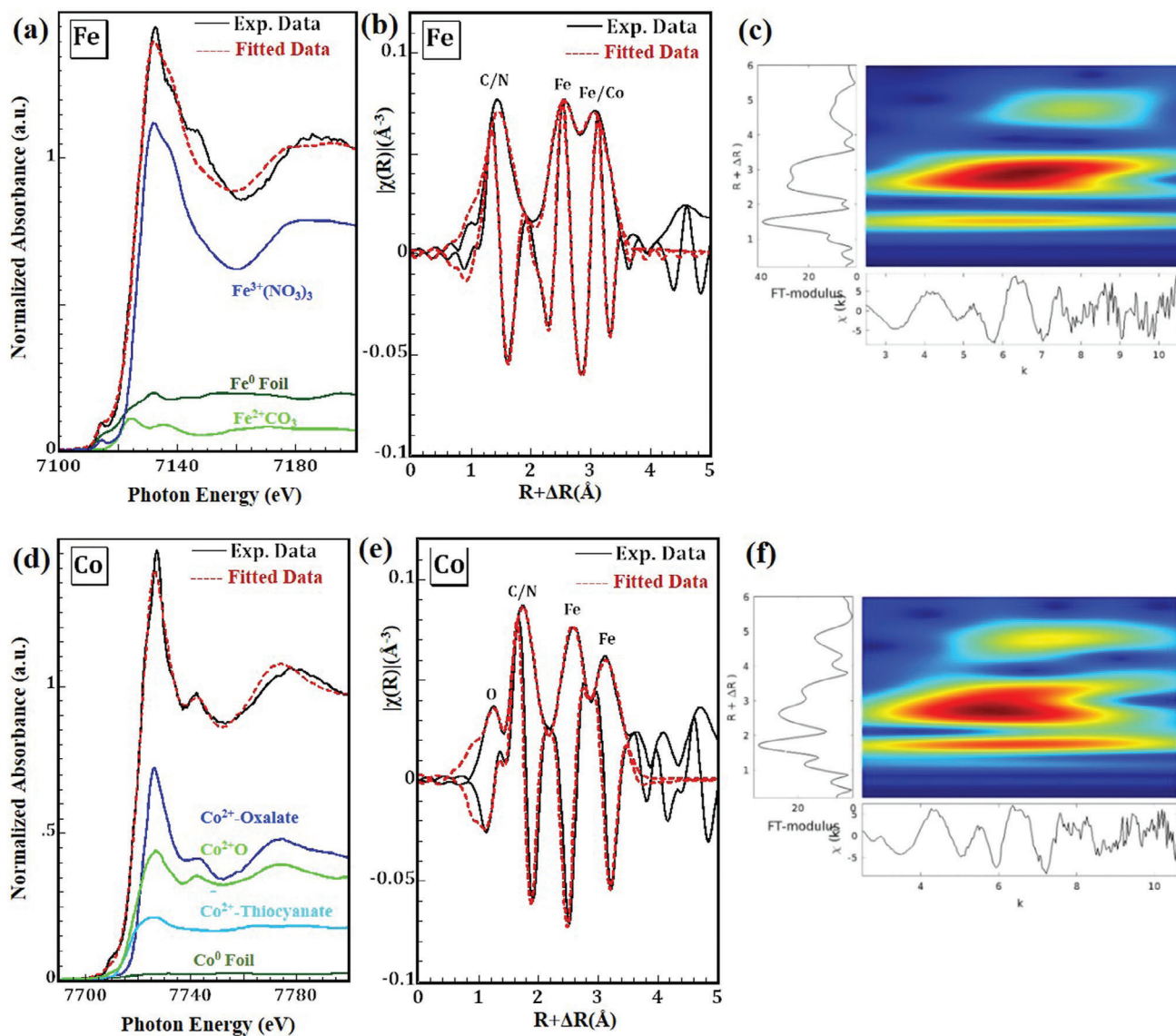


Figure 4. Figure 4. Linear Combination Fitting of the XANES data collected at the a) Fe K-edge and d) Co K-edge comparing different ratios of the used standards. EXAFS fitting of the amplitude and real part of the Fourier transformed EXAFS signal collected at the b) Fe K-edge and e) Co K-edge. Cauchy wavelet in k and R showing the type of the neighboring backscatters around c) Fe and e) Co atoms.

to be synthesized with 75 mM FeCl_3 and 25 mM $\text{Co}(\text{NO}_3)_2$ final concentrations.

In order to optimize the performance of the FeCoSAN, a pre-treatment of the electrodes was conducted by running 6 cycles of CV over a potential window ranging from 0.0 to -1.50 V in PBS solution (pH 5.0). Afterwards, the electrodes were rinsed with DI water and DPV was conducted in the presence of 500 μM nitrite. As can be seen in Figure S8a,b (Supporting Information), both, the control LSG and the FeCoSAN electrode showcased smaller peak currents after the pre-treatment. This is attributed to the reduction of some oxygen-containing functional groups present on the material, which are known to facilitate electron transfer processes. Nonetheless, the peaks became narrower, attributed to a decrease of the capacitive current, therefore, an enhanced signal-to-noise ratio, facilitating the specific determination of the target

analyte. Then, the pH of the buffer solution with the analyte was also optimized by adding either H_2SO_4 or KOH to obtain more acidic or basic pH values respectively. A pH of 7 was set as the starting point, and as can be appreciated in Figure S8c,d (Supporting Information) at higher values (9) the efficiency of the sensor decreased, therefore, lower values were tested. For pH 5.0 and 3.0, the recorded current magnitude had almost the same values, therefore, the former was selected as the optimal condition as it is closer in value to a neutral pH, commonly found on bodily fluids.

Next, the CV of three different FeCoSAN electrodes was measured in the presence of 5.0 mM $\text{K}_3\text{Fe}(\text{CN})_6$ dissolved in 0.1 M KCl at different scan rates between 100 and 1000 mV s^{-1} . Then, the anodic (I_{pa}) and cathodic (I_{pc}) peak currents were employed to obtain a calibration plot correlating the current response with the square root of scan rate. The corresponding

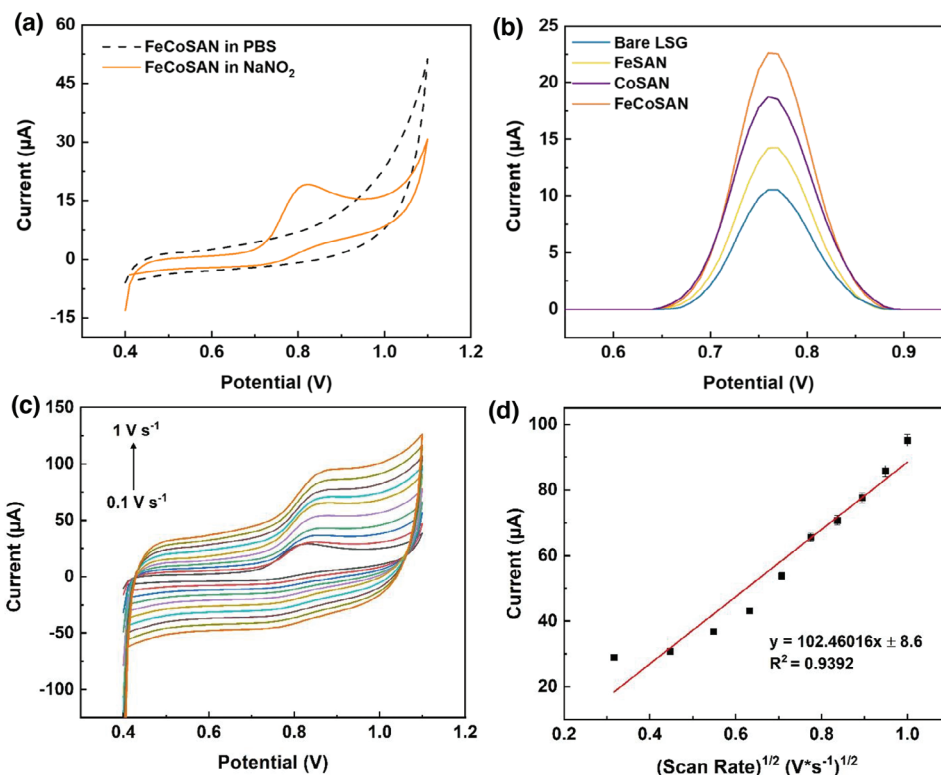


Figure 5. a) CV responses of FeCoSAN electrode in the presence of 500 μM NaNO_2 and PBS b) Comparison of current response of the FeCoSAN electrode to those obtained from bare LSG, FeSAN, and CoSAN in the presence of 500 μM NaNO_2 . c) CV responses of the FeCoSAN electrode at different scan rates in the presence of 500 μM NaNO_2 . d) Plot between current and square root of scan rate for CV responses of the FeCoSAN electrode at different scan rates.

linear equations are given in Figure S9 (Supporting Information). The obtained slope values of both, anodic and cathodic segments, were utilized in the Randles–Sevcik Equation to determine the electrochemically active surface area (ECSA) of the electrodes.

$$I_p = 2.69 \times 10^5 \cdot n^{3/2} \cdot A \cdot D^{1/2} \cdot C \cdot \nu^{1/2} \quad (1)$$

Where I_p is peak current, A is active surface area of the electrode, D is the diffusion coefficient ($D = 7.3 \times 10^{-6} \text{ cm}^2 \text{ s}^{-1}$), C is the concentration of $[\text{Fe}(\text{CN})_6]^{3-}$ ($C = 5 \times 10^{-6} \text{ mol cm}^{-3}$), and ν = scan rate (0.05 V s^{-1}). The average ECSA across the three electrodes was determined to be 0.1162 cm^2 , which represents a 63.66% increase over its geometrical surface area (0.071 cm^2).

2.3. Electrochemical determination of nitrite

The cyclic voltammetry of the FeCoSAN electrode was recorded employing phosphate buffer saline solution (pH 5) as the supporting electrolyte in the presence of 500 μM of NaNO_2 . As can be seen in Figure 5a, no peaks are present on the voltammogram without the analyte, however, with its addition, a clear anodic peak is observed with onset and peak potential set on 0.72 V and 0.82 V correspondingly. Then, to demonstrate the superior efficiency of the bimetallic material, the current response of its constituent individual elements was recorded. In Figure 5b, it can be observed that the FeCoSAN showcased a 100% increment in current with respect to the bare LSG electrodes and a

58% and 20% increase in comparison to the FeSAN and CoSAN, respectively. This enhancement in performance is attributed to the synergistic interaction between Co and Fe sites, as the incorporation of the more electronegative Co atoms improves the electronic structure, promoting a faster and more efficient electron transfer.^[40,41] By testing the electrode at different scan rates, from 300 to 1000 mV s^{-1} , a linear trend was observed between the square root of the scan rate and the current response suggesting a diffusion-controlled process. (Figure 5c,d)

The sensitivity of the FeCoSAN electrodes was studied by conducting chronoamperometry. As can be seen in Figure 6a (orange colored line), clear steps were recorded with the addition of each aliquot of NaNO_2 . The steady state current values of each step were employed to obtain the calibration plot in Figure 6b (orange colored line). The sensitivity of the electrode was determined by ratioing the slope of the linear fit over the geometrical surface area, yielding a value of $515.0704 \mu\text{A mm}^{-1} \text{ cm}^{-2}$. Next, the limit of detection ($\text{LoD} = 3.3\sigma/S$) of the electrode was calculated employing the standard deviation of the blank ($n = 10$) as σ and the slope of the linear fit as S . It was found that the system performed over a linear range from 5.0 to 1666 μM with an LoD of 2.42 μM . A comparison of the performance parameters of FeCoSAN with some reported systems based on Fe, Co and/or graphene is presented on Table S4 (Supporting Information). As can be seen, our material possesses an outstanding sensitivity in comparison with the other systems, only drastically surpassed by one material based on Co_3O_4 nano spindles/reduced graphene

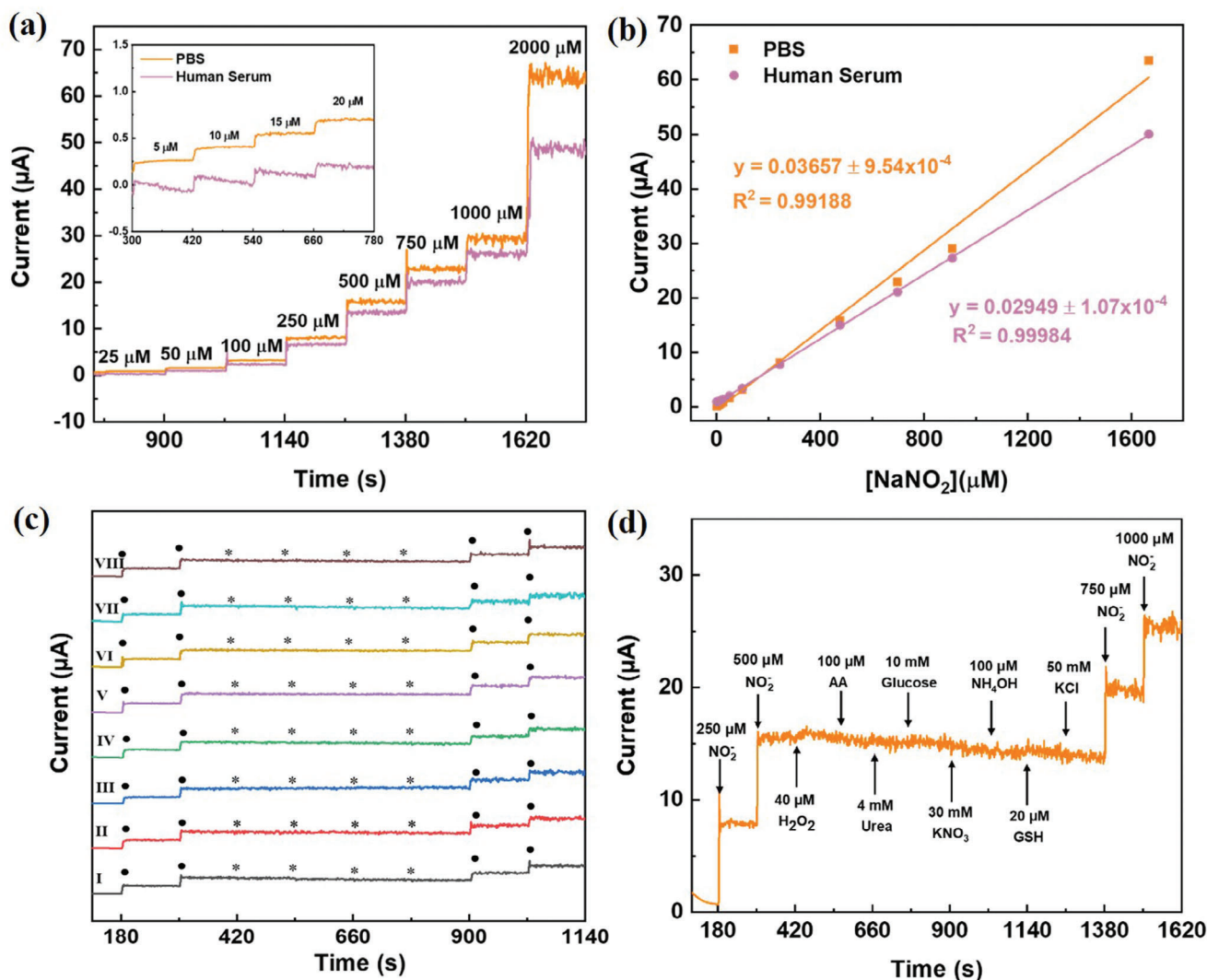


Figure 6. a) Comparison of amperometric signals of the FeCoSAN in PBS and artificial human serum (5%) to the addition of NaNO_2 aliquots. b) Corresponding calibration curves of the FeCoSAN electrode on PBS and artificial human serum (5%) c) Selectivity testing of individually tested FeCoSAN electrodes to common interferents under their physiological concentration ranges: (I) potassium chloride (10, 50, 75, 100 mM), (II) potassium nitrate (5, 10, 20, 30 mM), (III) ascorbic acid (25, 50, 75, 100 μM), (IV) glucose (1, 3, 5, 10 mM), (V) hydrogen peroxide (10, 20, 30, 40 μM), (VI) ammonium hydroxide (40, 60, 80, 100 μM), (VII) urea (1, 2, 3, 4 mM), (VIII) glutathione (5, 10, 15, 20 μM). Each dot (•) corresponds to the addition of 250 μM of NaNO_2 while every star (*) corresponds to the spiking of each interferent as listed previously. d) Amperometric signal of the FeCoSAN electrode with the consecutive addition of common interferents.

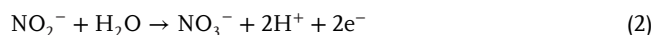
oxide. It's worth mentioning that regardless of the high sensitivity of said system, our material performs over a wider linear range. In addition, our sensing doesn't rely on the functionalization of a commercial electrode (GCE), therefore, simplifying the fabrication process and synthesis time.

The performance of the electrode as a real-world sensor was studied by recording its current-time response in the presence of 5% artificial human serum sample. The same procedure was conducted as previously described. As can be seen on Figure 6a (pink line), with the spiking of NaNO_2 , consistent steps were observed. The slope of the linear fit (Figure 6b, pink line) was employed to determine the sensitivity in this complex media, yielding a value of $415.3521 \mu\text{A mm}^{-1} \text{cm}^{-2}$, suggesting a 19.36% loss with respect to the performance on PBS.

The selectivity of the material to NaNO_2 was tested in the presence of different interferents commonly associated with nitrites such as glutathione, urea, ammonium hydroxide, hydrogen peroxide, glucose, ascorbic acid, potassium nitrate, and potassium chloride. As can be seen in Figure 6c, there were no steps to be appreciated with the spiking of each interferent, however, only a small decrease in current was observed with the addition of 50 mM of potassium chloride, which could be attributed to some fouling occurring on the surface of the electrode due to the high concentration of the interferent. In order to test the interference of these substances as a complex media, the highest tested concentration of each of them, up to the point where there was no decrease in current magnitude, was consecutively spiked as can be seen in Figure 6d. As expected, no signals were recorded for

the addition of the individual interferents, however, a smaller current was recorded with the addition of 750 μM NaNO_2 than that obtained with the previously added aliquots of the same magnitude (250 and 500 μM), suggesting a certain degree of interference, similarly to the case of artificial human serum. Nonetheless, it is worth noting the efficiency of the system for detecting the desired analyte even under the presence of such a complex medium.

A characteristic oxidation signal observed at +0.70 V (vs. Ag/AgCl), which corresponds to the anodic conversion of NO_2^- to nitrate (NO_3^-) through a second-order homogeneous disproportionation process, as reported by Guidelli et al.^[42] This process follows an ECE mechanism, where the overall reaction can be expressed as, Equation (2),



At the FeCoSAN interface, NO_2^- molecules undergo electron transfer, forming nitrite radicals (NO_2^\cdot). These NO_2^\cdot then chemically react with another NO_2^- , producing nitrate (NO_3^-) and nitric oxide (NO). The NO generated in this step undergoes further oxidation to NO_3^- in the final electrochemical step.^[43] The FeCoSAN catalyst, with its single-atom (Fe or Co) active sites, plays a crucial role in facilitating the oxidation process. The single-atom sites provide specific active sites for the adsorption and activation of NO_2^- molecules, enhancing the initial electron transfer step. Additionally, the dual-atom Fe-Co pair could offer synergistic activity in catalyzing the reactions. Furthermore, the well-dispersed single-atom sites in FeCoSAN facilitate efficient electron transfer, leading to enhanced current signals and improved sensitivity of the sensor. Moreover, the highly porous structure of laser-produced graphene sheets contributes additional active sites for the adsorption and oxidation of nitrite to nitrate, as extensively documented in the literature.^[44]

The interaction of various interferents with the FeCoSAN sensor can be categorized as either physical adsorption or chemical interaction. Species like potassium nitrate and potassium chloride are primarily physically adsorbed due to weak electrostatic interactions and do not undergo significant reactions with the active sites. In contrast, interferents such as ascorbic acid, glucose, and hydrogen peroxide may chemically interact with the Fe, Co, or Fe-Co active sites through redox processes. However, the applied potential of +0.70 V (vs. Ag/AgCl) is optimized to selectively oxidize NO_2^- , minimizing interference from these species. The high selectivity of FeCoSAN arises from its single-atom and dual-atom active sites, which preferentially adsorb and catalyze the oxidation of nitrite.

The repeatability of the FeCoSAN was studied by recording the differential pulse voltammetry signal of five different electrodes, by triplicate, in the presence of 1mM NaNO_2 . The resulting voltammograms were normalized by performing a moving average baseline subtraction. The averaged signal of the three measurements per electrode is showcased on Figure S10a,b (Supporting Information), along with a bar chart plot exhibiting the peak current attributed to each electrode. The average current across the tested electrodes was found to be 32.14175 μA with a standard deviation and relative standard deviation of 2.35 μA and 7.33% respectively. This value suggests a fairly reproducible system. Lastly, the stability of the FeCoSAN electrode was studied

by recording its differential pulse voltammetry response in the presence of 1 mM NaNO_2 every seven days for four weeks. The voltage window was set from +0.45 to +1.0 V. Similarly to the repeatability tests, three runs were conducted, normalized, and averaged. The peak currents were plotted on a bar chart against time of measurement (Figure S11, Supporting Information). The shelf-life stability was assessed by comparing the current values obtained on the first (31.89 μA) and last day (25.55 μA), suggesting a shelf-life stability of 82.93%, therefore, only a 17% efficiency loss after a month of exposing the electrode to atmospheric conditions.

3. Conclusion

In summary, we successfully synthesized a bimetallic (Fe:Co) graphene-supported single-atom catalyst using a laser-assisted method with minimal solution processing. The successful loading of the metal atoms was confirmed through HAADF-STEM, EELS, EXAFS, and XANES analyses. ICP-OES was employed to estimate the metal loading, revealing values of 1.135 wt% for iron and 0.336 wt% for cobalt, with an average Fe:Co ratio of 3.38. When utilized as a working electrode, the material demonstrated excellent capabilities for nitrite determination, achieving a detection limit as low as 2.42 μM and a sensitivity of 515.07 $\mu\text{A mm}^{-1} \text{cm}^{-2}$. The bimetallic FeCoSAN surpasses the efficiency of its individual components (LSG, FeSAN, and CoSAN) by considerable percentages (100%, 58%, and 20% respectively). The effective synthesis of this material highlights the potential of the employed technique to design and synthesize various bimetallic materials by simply exchanging the metallic components, offering significant promise for a wide range of applications, from clinical diagnostics to food industry.

4. Experimental Section

Materials: Cobalt (II) nitrate hexahydrate ($\text{Co}(\text{NO}_3)_2 \cdot 6\text{H}_2\text{O}$), polyvinyl alcohol (PVA), hydrogen peroxide solution (H_2O_2 , 30 wt%), dopamine hydrochloride, D-glucose, and human serum from human male AB plasma were acquired from Sigma-Aldrich. Iron (III) chloride hexahydrate ($\text{FeCl}_3 \cdot 6\text{H}_2\text{O}$) was obtained from VWE Chemicals. Sodium nitrite (NaNO_2), potassium Chloride (KCl) and potassium nitrate (KNO_3) were purchased from Fisher Chemical. Glutathione reduced (GSH) was acquired from Fisher Bioreagents. Ammonium hydroxide solution (NH_3 28.0-30.0%) was obtained from Honeywell. Potassium ferricyanide ($\text{K}_3[\text{Fe}(\text{CN})_6]$), and potassium chloride (KCl) and phosphate-buffered saline (PBS) tablets containing 0.0027 M KCl and 0.137 M sodium chloride were acquired from MP Biomedicals. Commercial polyimide (PI) sheets (Kapton Width: 12) were purchased from Utech Products. Ultrapure water (resistivity: 18.2 $\text{M}\Omega \cdot \text{cm}^{-1}$ at 25°C) from a GenPurePro UV integral water purification system (ThermoScientific) was used in all aqueous solution experiments. All the chemicals were of analytical grade and used as received without any prior treatment. Stock solutions were freshly prepared prior to their employment.

Instrumentation: Laser scribing was conducted employing a Universal Laser Systems® (PLS6.75). Scanning electron microscopy was conducted with a Zeiss Merlin field-emission microscope. High-angle annular dark-field scanning transmission electron microscopy (HAADF-STEM) imaging, Electron energy loss spectroscopy (EELS), and Energy-dispersive X-ray spectroscopy (EDS) were performed employing a Thermo Fisher Scientific Titan Cubed TEM (80-300 keV), attached with a Probe Cs corrector, a high-brightness electron gun (x-FEG), and four in-column 4 SDD Super-X

detectors. X-ray photoelectron spectroscopy (XPS) measurements were carried out in a Kratos Axis Supra DLD spectrometer attached to a monochromatic Al K α X-ray source ($h\nu = 1486.6$ eV) operating at 75 W under high vacuum conditions. XPS survey and high-resolution spectra were collected with fixed analyzer pass energies of 160 eV. X-ray diffraction (XRD) was performed with a Bruker Corporation, D8 ADVANCE diffractometer with Cu K α radiation (1.5406 Å). Data was collected over a 2θ range of 5–80°. Raman spectroscopy was conducted employing a Horiba Scientific, Alpha3000 Ayrton Witec Raman spectrometer coupled with a 532.163 nm laser excitation source at room temperature. X-ray absorption spectroscopy (EXAFS and XANES) was performed on the BM08-XAFS/XRF beamline at the Synchrotron-light for Experimental Science and Applications in the Middle East (SESAME).^[45] The FeCoSAN sample was pressed into pellet form after scratching the material from the PI substrate, grounding it and mixing ≈ 65 mg of it with polyvinylpyrrolidone (PVP) binder. XANES and EXAFS spectra were acquired at ambient room temperature in step-by-step scanning mode using a double crystal monochromator equipped with Si (111) crystal achieving an energy resolution ΔE of $\approx 2.4 \times 10^{-4}$ eV. The transmission mode was used for collecting XAFS data at the Fe and Co K-edges using ionization chambers filled with adequate mixed noble gases. The energy was calibrated at the Fe K-edge (7112.0 eV) and Co K-edge (7708.9) of the Fe and Co standard metal foils. Collected data was processed and analyzed using Demeter (Athena) and WinXAS software packages.^[46,47] XANES features are compared to different references to determine the redox state. In addition, a linear combination fitting approach (LCF) was performed considering different reference model compounds. In a different way, and for quantitative EXAFS data analysis, the experimental spectra have to be compared with the theoretically calculated ones by using the ab initio FEFF code for EXAFS calculation.^[48] The crystal structure parameters of theoretical reference models Fe metal, Co metal, FeCo, FeCo₃N₃, FeN, Fe₃C, FeO, Fe₂O₃, Co₂C, CoO, Co₃FeN₃, etc from the crystallography open database. Inductively Coupled Plasma-Optical Emission Spectroscopy (ICP-OES) was performed with a 5100 ICP-OES Agilent instrument. Powder samples were scratched from the PI substrate and 8–10 mg were set for digestion on an UltraWAVE instrument (Milestone) at 240 °C and 35 bar for 30 min, using an acid solution containing 3.0 mL HCl + 1.0 mL HNO₃ + 1.0 mL HF. Later, 5.0 mL of the digested sample was placed on a falcon tube with 5.0 more mL of HNO₃. Digested samples were measured by quintupled for each of the 10 selected emission wavelengths (Five for Fe and five for Co). Lastly, 1.0 mL of each evaluated sample was further diluted with 9.0 mL of HNO₃ and measured once more by quintupled per wavelength. Standard solutions with different concentrations of Fe and Co were previously prepared, obtaining proper calibration curves with $R^2 > 0.999$. Moreover, laboratory reagent blank (LRB), laboratory fortified blank (LFB) and quality control sample (QCS) were evaluated to validate the results.

Fabrication of FeCoSANs: For the optimized version of the material, a metallic slurry was prepared by ultrasonically, at a frequency of 45 kHz, 5 mL of polyvinyl alcohol (PVA) in water (15% wt.), 1.875 mL of iron chloride solution (400 mM), 1.25 mL of cobalt nitrate solution (200 mM), 1.875 mL of DI water and 1.0 g of urea for 10 min. Simultaneously, the polyimide (PI) sheets (6.3 × 3.5 cm) were ultrasonically cleaned with acetone for 10 min and subjected to oxygen plasma treatment for 10 min. The as-prepared solution (1.0 mL per substrate) was immediately blade coated (1000 μ m height) onto the pre-cleaned PI sheets at a 20 mm s⁻¹ speed. Then, substrates were annealed until a dry film was observed. A CO₂ laser was used to scribe circular working electrodes with a 3 mm diameter on the metallic slurry-coated sheets. The parameters were set as follows: 2.8 W power, 4.5 cm s⁻¹ speed, 1000 pulses per inch, and 1.0 mm Z distance. To reduce contact resistance with the utilized screen-printed electrode connectors (SPE connector, 4 mm banana), the contacts were sputtered with 200 nm of silver. To serve as control, bare LSG electrodes were prepared following the same procedure, skipping the blade coating and annealing steps.

Electrochemical Experimental Procedure: All electrochemical measurements were carried out using 0.1 M phosphate buffer saline (PBS, pH 5) as the supporting electrolyte at ambient conditions, after the pH optimization tests. Prior to those tests, PBS pH 7.4 was employed. A three-electrode system consisting of LSG or FeCoSAN as working electrode, a platinum

wire as counter electrode and a silver/silver chloride (Ag/AgCl) as reference electrode was utilized. The electrochemical cell volume was 20 mL for all amperometry experiments and 10 ml for all voltammetry experiments. Cyclic voltammetry (CV) tests were conducted between +0.30 to 1.20 V at a 50 mV s⁻¹ scan rate, unless specified. Differential pulse voltammetry (DPV) was conducted between +0.45 to +1.0 with a scan rate of 0.20 V, a pulse time of 0.6 s and a scan rate of 50 mV s⁻¹. The chronoamperometry tests were conducted at a fixed potential of +0.82 V and the sampling interval for each subsequent aliquot was 2 min. Prior to any measurement, pretreatment of the electrodes was conducted through electrochemical reduction by performing 6 subsequent cycles of cyclic voltammetry at a 100 mV s⁻¹ scan rate over a potential window of 0.0 to -1.50 V as indicated on the corresponding section.

Supporting Information

Supporting Information is available from the Wiley Online Library or from the author.

Acknowledgements

This work was supported financially by the King Abdullah University of Science and Technology (KAUST), Saudi Arabia. In addition, The authors acknowledge the funding from the KAUST smart health initiative. We thank the KAUST Core Lab teams for their help on the materials characterization raw data, especially to Georgian Melinte and Mohamed Nejib. G.T.B. is thankful to Prof. Derya Baran for providing facilities to conduct the blade coating of the materials.

Open access publishing facilitated by King Abdullah University of Science and Technology, as part of the Wiley – King Abdullah University of Science and Technology (KAUST) agreement.

Conflict of Interest

The authors declare no conflict of interest.

Data Availability Statement

The data that support the findings of this study are available from the corresponding author upon reasonable request.

Keywords

bimetallic, laser scribed graphene, oxidative stress, reactive nitrogen species, single-atom catalyst

Received: September 6, 2024

Revised: January 20, 2025

Published online:

- [1] J. O. Lundberg, E. Weitzberg, *Cell* **2022**, *185*, 2853.
- [2] J. O. Lundberg, M. T. Gladwin, A. Ahluwalia, N. Benjamin, N. S. Bryan, A. Butler, P. Cabrales, A. Fago, M. Feilisch, P. C. Ford, B. A. Freeman, M. Frenneaux, J. Friedman, M. Kelm, C. G. Kevil, D. B. Kim-Shapiro, A. V. Kozlov, J. R. Lancaster, D. J. Lefer, K. McColl, K. McCurry, R. P. Patel, J. Petersson, T. Rassaf, V. P. Reutov, G. B. Richter-Addo, A. Schechter, S. Shiva, K. Tsuchiya, E. E. van Faassen, A. J. Webb, B. S. Zuckerbraun, J. L. Zweier, E. Weitzberg, *Nat. Chem. Biol.* **2009**, *5*, 865.

- [3] E. Lubos, D. E. Handy, J. Loscalzo, *Front Biosci.* **2008**, *13*, 5323.
- [4] E. Tatsch, G. V. Bochi, R. d. S. Pereira, H. Kober, V. A. Agertt, M. M. Anraku de Campos, P. Gomes, M. M. M. F. Duarte, R. N. Moresco, *Clin. Biochem.* **2011**, *44*, 348.
- [5] T. Wei, C. Chen, J. Hou, W. Xin, A. Mori, *Biochimica et Biophysica Acta (BBA) – Mol. Cell Res.* **2000**, *72*, 1498.
- [6] L. Ma, L. Hu, X. Feng, S. Wang, *Aging Dis.* **2018**, *9*, 938.
- [7] F. T. S. M. Ferreira, R. B. R. Mesquita, A. O. S. S. Rangel, *Talanta* **2020**, *219*, 121183.
- [8] J. S. W. Chui, W. T. Poon, K. C. Chan, A. Y. W. Chan, T. A. Buckley, *Anaesthesia* **2005**, *60*, 496.
- [9] F. A. Ansari, S. N. Ali, R. Mahmood, *Toxicol. In Vitro* **2015**, *29*, 1878.
- [10] Y. Sun, H. Xu, D. Zhou, C. Xia, W. Liu, A. Cui, Z. Wang, W. Zheng, G. Shan, J. Huang, X. Wang, *Small* **2024**, *20*, 2309357.
- [11] L. Bellavia, D. B. Kim-Shapiro, S. B. King, *Future Sci. OA* **2015**, *1*, FSO36.
- [12] R. Gaikwad, P. R. Thangaraj, A. K. Sen, *Analyst* **2022**, *147*, 3370.
- [13] B. R. Kozub, N. V. Rees, R. G. Compton, *Sens., Actuat. B: Chem.* **2010**, *143*, 539.
- [14] Q.-H. Wang, L.-J. Yu, Y. Liu, L. Lin, R.-G. Lu, J.-P. Zhu, L. He, Z.-L. Lu, *Talanta* **2017**, *165*, 709.
- [15] J. Liu, L. Gong, H. Chen, J. Gui, X. Zhu, M. Liu, Y. Zhang, S. Yao, *ACS Appl. Nano Mater.* **2023**, *6*, 5879.
- [16] A. Kumar, V. Q. Bui, J. Lee, L. Wang, A. R. Jadhav, X. Liu, X. Shao, Y. Liu, J. Yu, Y. Hwang, H. T. D. Bui, S. Ajmal, M. G. Kim, S.-G. Kim, G.-S. Park, Y. Kawazoe, H. Lee, *Nat. Commun.* **2021**, *12*, 6766.
- [17] S. Wang, H. Gao, L. Li, K. S. Hui, D. A. Dinh, S. Wu, S. Kumar, F. Chen, Z. Shao, K.N. Hui, *Nano Energy* **2022**, *100*, 107517.
- [18] M. Zhao, R. Yang, Y. Wei, J. Su, X. Wang, N. Zhang, P. Sun, D. Chen, Y. Zhao, *Nano Today* **2022**, *44*, 101493.
- [19] C. Xu, L. Liu, X. Zhang, L. Guo, X. Zhang, Z. Huang, X. Wu, H. Zhao, G. Jing, H. Shen, *Chem. Eng. J.* **2024**, *480*, 148361.
- [20] V. Giulimondi, A. RuizFerrando, A. H. Clark, S. K. Kaiser, F. Krumeich, A. J. Martín, N. López, J. PérezRamírez, *Adv. Funct. Mater.* **2022**, *32*, 2206513.
- [21] Z. Hou, L. Dai, Y. Liu, J. Deng, L. Jing, W. Pei, R. Gao, Y. Feng, H. Dai, *Appl. Catal., B* **2021**, *285*, 119844.
- [22] Z. Xu, Q. Zhang, Z. Huang, H. Chen, J. Zhang, W. Chen, G. Meng, D. Wang, *Sci. China: Chem.* **2023**, *66*, 1241.
- [23] W. Liu, H. Feng, Y. Yang, Y. Niu, L. Wang, P. Yin, S. Hong, B. Zhang, X. Zhang, M. Wei, *Nat. Commun.* **2022**, *13*, 3188.
- [24] M. Yang, B. Li, S. Li, Q. Dong, Z. Huang, S. Zheng, Y. Fang, G. Zhou, X. Chen, X. Zhu, T. Li, M. Chi, G. Wang, L. Hu, Z. J. Ren, *Nano Lett.* **2023**, *23*, 7733.
- [25] V. B. Saptal, V. Ruta, M. A. Bajada, G. Vilé, *Angew. Chem., Int. Ed.* **2023**, *62*, 202219306.
- [26] Z. Zheng, L. Qi, X. Luan, S. Zhao, Y. Xue, Y. Li, *Nat. Commun.* **2024**, *15*, 7331.
- [27] S. Rauf, A. A. Lahcen, A. Aljedaibi, T. Beduk, J. Ilton de Oliveira Filho, K. N. Salama, *Biosens., Bioelectron.* **2021**, *180*, 113116.
- [28] A. Ghanam, A. A. Lahcen, T. Beduk, H. N. Alshareef, A. Amine, K. N. Salama, *Biosens., Bioelectron.* **2020**, *168*, 112509.
- [29] G. Tostado-Blazquez, S. S. Shetty, S. Yuvaraja, J. L. Cerrillo, V. Mani, K. N. Salama, *Small Sci.* **2024**, *4*, 2300259.
- [30] G. Tostado-Blazquez, S. S. Shetty, S. Yuvaraja, J. L. Cerrillo, V. Mani, K. N. Salama, *ACS Appl. Nano Mater.* **2024**, *7*, 17611.
- [31] A. A. Lahcen, S. Rauf, T. Beduk, C. Durmus, A. Aljedaibi, S. Timur, H. N. Alshareef, A. Amine, O. S. Wolfbeis, K. N. Salama, *Biosens., Bioelectron.* **2020**, *168*, 112565.
- [32] K. S. Loh, S. Samad, Y. Yusoff, W. Wong, *J. Kejuruteraan* **2018**, *1*, 31.
- [33] J. Wang, R. You, C. Zhao, W. Zhang, W. Liu, X.-P. Fu, Y. Li, F. Zhou, X. Zheng, Q. Xu, T. Yao, C.-J. Jia, Y.-G. Wang, W. Huang, Y. Wu, *ACS Catal.* **2020**, *10*, 2754.
- [34] M. Basak, M. L. Rahman, M. F. Ahmed, B. Biswas, N. Sharmin, *J. Alloys, Compounds* **2022**, *895*, 162694.
- [35] W. Zhang, C.-H. Xu, H. Zheng, R. Li, K. Zhou, *Adv. Funct. Mater.* **2022**, *32*, 2200763.
- [36] G. Wan, P. Yu, H. Chen, J. Wen, C.-J. Sun, H. Zhou, N. Zhang, Q. Li, W. Zhao, B. Xie, T. Li, J. Shi, *Small* **2018**, *14*, 1704319.
- [37] H. Wu, G. Gao, X. Zhou, Y. Zhang, S. Guo, *Cryst. Eng. Commun.* **2012**, *14*, 499.
- [38] X. Zeng, J. Shui, X. Liu, Q. Liu, Y. Li, J. Shang, L. Zheng, R. Yu, *Adv. Energy Mater.* **2018**, *8*, 1701345.
- [39] X. Li, A.-E. Surkus, J. Rabeah, M. Anwar, S. Dastagir, H. Junge, A. Brückner, M. Beller, *Angew. Chem., Int. Ed.* **2020**, *59*, 15849.
- [40] K. Liu, Y. Chen, X. Dong, Y. Hu, H. Huang, *Electrochim. Acta* **2023**, *456*, 142441.
- [41] Y. Huang, J. Xiong, Z. Zou, Z. Chen, *Adv. Mater.* **2025**, *37*, 2312182.
- [42] R. Guidelli, F. Pergola, G. Raspi, *Anal. Chem.* **1972**, *44*, 745.
- [43] V. Mani, A. P. Periasamy, S.-M. Chen, *Electrochem. Commun.* **2012**, *17*, 75.
- [44] X. Li, J. Ping, Y. Ying, *TrAC, Trends Anal. Chem.* **2019**, *113*, 1.
- [45] M. Harfouche, M. Abdellatif, Y. Momani, A. Abbadi, M. Al Najdawi, M. Al Zoubi, B. Aljamil, S. Matalgah, L. U. Khan, A. Lausi, G. Paolucci, *J. Synchrotron Radiat.* **2022**, *29*, 1107.
- [46] T. Ressler, *J. Synchrotron Radiat.* **1998**, *5*, 118.
- [47] B. Ravel, M. Newville, *J. Synchrotron Radiat.* **2005**, *12*, 537.
- [48] J. J. Rehr, R. C. Albers, *Rev. Mod. Phys.* **2000**, *72*, 621.